

# Deep learning and correlative microscopy for quantification of grain orientation in sintered FeNdB-type permanent magnets by domain pattern analysis

Amit Kumar Choudhary<sup>a,b,\*</sup>, Tvrtko Grubesa<sup>a,b</sup>, Andreas Jansche<sup>a</sup>, Timo Bernthaler<sup>a</sup>, Dagmar Goll<sup>a</sup>, Gerhard Schneider<sup>a,b</sup>

<sup>a</sup> Materials Research Institute, Aalen, Germany

<sup>b</sup> Karlsruhe Institute of Technology, Karlsruhe, Germany

## ARTICLE INFO

### Keywords:

Deep learning  
Kerr microscopy  
EBSD  
Regression task  
Permanent magnets  
Magnetic domains  
Grain orientation  
Correlative microscopy  
Crystal orientation

## ABSTRACT

Based on a data-driven approach, a computer-assisted workflow for the quantitative analysis of optical Kerr microscopy images of sintered FeNdB-type permanent magnets was developed. By analyzing the domain patterns visible in the Kerr image with data-driven approaches such as traditional machine learning and advanced deep learning, we can quantify grain orientation and size with a better trade-off between accuracy and higher throughput than electron backscatter diffraction (EBSD). The key distinction between traditional machine learning and advanced deep learning lies in feature extraction. Traditional methods require manual, user-dependent feature extraction from input data, while advanced deep learning achieves this automatically. The predictions from the trained models were compared to the measurements from EBSD for performance evaluation. The proposed data-driven model is trained on the dataset created from the correlative microscopy technique, which requires the images of grains extracted from the Kerr microscopy and corresponding EBSD grain orientation data (Euler angles). The fine-tuned deep learning model shows better generalization ability than the traditional machine learning models trained on the manually extracted features and resulted in a mean absolute error of less than 5° for grain orientation of the anisotropic magnet samples when evaluated against the measured EBSD values. The developed approach has reduced the measurement effort for grain orientation by 5 times and have sufficient accuracy when compared to the EBSD.

Further, the application of the proposed approach to determine the quality of the alignment or texture in anisotropic sintered magnets and its relationship with the magnetic remanence based on reliable statistical grain orientation data has been discussed. This approach could emerge as a tool for rapidly analyzing large-scale samples to discover and quantify heterogeneities in grain size and grain orientation.

## 1. Introduction

Microstructural analysis using microscopy has been integral to materials research for decades. Its possibilities have been increased by the availability of new signal generation and acquisition technologies based on various physical interaction principles. Within each technology, the developers have aimed to improve sensitivity and resolution while defining quantification methods that rely on computer-assisted workflows.

This paper presents a workflow for the computer-assisted quantification of grain orientation based on images acquired using Kerr

microscopy (KM). This workflow incorporates a performance comparison between machine learning (ML) and deep learning (DL)-based models, which quantify the three-dimensional grain orientation and grain size of the hard-magnetic phase in sintered FeNdB magnets in their thermally demagnetized state from light optical microscopy data under polarized light. Both ML and DL based models were trained on the same training dataset, which combines electron backscatter diffraction orientation data and the correlative Kerr microscopy image of the magnet samples, accounting for more than 4000 grains of different orientations. The test set samples for evaluating the model performance and determining generalization ability are manufactured using different

\* Corresponding author.

E-mail address: [amit.kumar.choudhary@hs-aalen.de](mailto:amit.kumar.choudhary@hs-aalen.de) (A.K. Choudhary).

<https://doi.org/10.1016/j.actamat.2023.119563>

Received 26 May 2023; Received in revised form 27 November 2023; Accepted 27 November 2023

Available online 28 November 2023

1359-6454/© 2023 The Authors. Published by Elsevier Ltd on behalf of Acta Materialia Inc. This is an open access article under the CC BY license (<http://creativecommons.org/licenses/by/4.0/>).

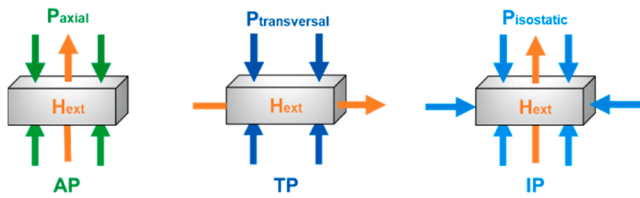


**Fig. 1.** Compaction of green body powder under mechanical pressure and particle alignment parallel to external magnetic field  $H_{\text{ext}}$  using different geometric configurations: axial (AP), transversal (TP), and isostatic (IP) compaction. (For interpretation of the references to colour in this figure legend, the reader is referred to the web version of this article.)

compaction methods, resulting in varying anisotropy or grain alignment. The degree of alignment is quantified as a function of grain orientation distribution, with statistics derived from it and correlated to the magnetic property.

### 1.1. Anisotropy of FeNdB-type permanent magnets

The manufacturing process for sintered permanent magnets leads to a complex microstructure that involves highly anisotropic grain alignment of the hard-magnetic phase with the composition FeNdB, ideally providing their magnetic decoupling via non-ferromagnetic grain boundary phases [1]. Different degrees of alignment is achieved depending on the green body powder compaction method [2]. Depending on the geometric arrangement of the pressing tool and the direction of the external magnetic field  $H_{\text{ext}}$ , axial (AP), transversal (TP), and isostatic (IP) compaction methods are used in industrial processes (schematically displayed in Fig. 1).

The magnetic field  $H_{\text{ext}}$  and pressing direction are crucial for the texture of the magnets. Due to mechanical influences from compaction forces, friction, and magneto-static effects between the particles (typical particle size 1–5  $\mu\text{m}$ ), alignment along magnetic field lines is obstructed. Since the powder particles' easy axes are aligned with the pressing direction, grain alignment gets affected during compaction due to friction. This friction exists between powder particles and also between particles and the die. Consequently, axial compaction results in higher grain misorientation than to transversal or isostatic compaction [2–4].

While IP compaction generally shows pronounced uniaxial texture with high homogeneity within the magnet volume, samples from TP and AP compaction may show some deviations from the uniaxial texture due to the geometric limitations of the process. Therefore, it is important to quantify the grain alignment or orientation on different length scales to assure the quality by analyzing the anisotropy using different techniques.

## 2. State-of-the-art technologies for quantifying anisotropy

### 2.1. Magnetometric characterization

Naturally, magnetic materials can be analyzed using magnetometric methods. Quantifying manufacturing inhomogeneities require analysis on a large scale, typically done by measuring the magnetic dipole moment of the magnet to its geometric axes. This procedure provides information on a global scale and requires the sample to be fully magnetized. Further, the measurement of remanence and coercivity is a crucial parameter for magnet performance, which is influenced by anisotropy.

### 2.2. Diffraction-based methods

For the microstructural quantification of grain orientation and size as well as for determining the material textures, SEM-EBSD mapping has emerged as a state-of-the-art technology. As a diffraction-based method,

it provides high accuracy. However, the diffraction-based methods are primarily suitable for analyzing the small areas within the samples [5]. Another established method is texture analysis by measuring pole figures using XRD. A more unusual approach to acquiring locally resolved texture information over large length scales is using macroscopic diffraction techniques, such as XRD, as suggested by Bunge [6].

Although valuable information about crystallographic anisotropy and homogeneity can be gained, this method does not provide information on the microstructural level. Therefore, better resolution on the microstructural level requires microscopy techniques.

### 2.3. Optical microscopy for crystallographic information

Kerr microscopy for permanent and soft magnetic materials is an established method for visualizing magnetic domain structures [7,8]. Furthermore, polarized light optical microscopy has been used to obtain the grain orientation of the metals with a hexagonal structure and for geological applications for a large specimen area [9–12]. Jin et al. in [13] determined the orientation of  $\alpha$ -titanium using polarized light optical microscopy and compared it against the EBSD approach. This approach involves a physics-based forward model that can simulate the interaction between the material with polarized light and predict the grain orientation. The deviation between the predicted and EBSD values was in the range of 2.5°–20°

Gaskey et al. in [14] characterized the crystal orientation of pure nickel coin and polycrystalline silicon solar cells using directional reflectance microscopy (DRM). DRM is an optical microscopy technique that captures the crystal lattice information as DRM maps when the sample is observed under a series of illumination from different angles. Using the mathematical analysis, a directional reflectance profile (DRP), and Funk-Radon transform (FRT), 3D orientation indexing is obtained, achieving a difference of 4°–10° against the EBSD. Similar works to retrieve partial grain orientation from the DRM have been carried out by Seita et al. [15] and Hara et al. [16].

Some of the other techniques to determine grain orientation from microscopy data are spatially resolved acoustic microscopy [17], Raman microscopy [18], and ultrasound methods [19].

### 2.4. Data-driven methods for microscopy-based crystallographic information

Recent developments in data-driven approaches and analysis have led to the application of state-of-the-art machine learning or deep learning techniques to accelerate the process of quantitative microstructure analysis, overcome the existing methods' challenges, and improve the material characterization process through crystallographic grain orientation analysis. DL-based models are trained to predict the orientation of the EBSD pattern indexes to overcome the challenges of traditional EBSD indexing [20–24].

Further, correlative microscopy data has been actively used, along with machine learning techniques to develop knowledge transfer functions from different microscopy methods [25–27]. In [19], Shen et al. used Raman-SEM-EDS data to classify the phases in the  $\text{WO}_3$ - $\text{WS}_2$  powder and volcanic rock samples using a random forest classifier. Wittwer et al. in [27] developed the EulerNet model to predict the crystal orientation of Inconel 718 using correlative microscopy data that includes directional reflectance microscopy and EBSD. DRM measures the local surface reflection intensity for different ranges of illumination angles as a 2D array of  $6 \times 72$  continuous values for each grain. The model takes input signals from DRM as a 2D array for each grain and maps it to the Euler angles obtained from the EBSD. The trained EulerNet resulted in a disorientation angle of 6.7° on the validation set.

### 3. Domain pattern analysis and crystallographic orientation measurement (DoPACOM)

In this work, grain orientation and size data are acquired using EBSD mapping to provide a ground truth for the training dataset. The Kerr microscopy image and corresponding SEM-EBSD mapping are acquired using the correlative microscopy technique. Fig. 2 shows the correlative microscopy image of the microstructure of a sintered FeNdB-type magnet with an axis of anisotropy (c-axis of grains) perpendicular to the image plane (a, b, c) and within the image plane (d, e, f). The direction of the external magnetic field used during the compaction and alignment process is indicated by “ $H_{ext}$ ”. The bright field microscopy images in Fig. 2(a) & (b) visualize the different phases, the grains of the hard-magnetic phase, pores, oxides, and the phases that form grain boundaries. By contrast, with Kerr microscopy, the domain structures within the hard-magnetic phases become visible. According to the domain structures grain orientations can be distinguished. Fig. 2(c) & (f) shows the EBSD mapping with IPF color coding representing the orientation of grains of the hard-magnetic phases.

Kerr microscopy is an optical technique that uses the magneto-

optical Kerr effect (MOKE) to visualize magnetic domains within grains up to  $0.1 \mu\text{m}$  spatial resolution. MOKE captures the interaction between the incident linearly polarized light and the magnetic stray fields on the surface of a ferromagnetic sample. The incident linear polarized light becomes elliptically polarized after reflection. With respect to the incident linear polarization plane, the major angle of the reflected polarized ellipse is called the Kerr rotation angle ( $\alpha_K$ ). The advantage over other methods is that large areas can be scanned in a short time to detect orientation differences within sintered components. This applies to both hard and soft magnetic materials.

The state of magnetization and orientation of the grain to the incident plane of the polarized light influences the rotation. In the case of thermally demagnetized FeNdB magnets, the grains provide no net magnetization. However, on a micromagnetic scale, the internal stray field minimization leads to the development of magnetic domains of opposite magnetization direction within the grain. It is essential that in materials with high uniaxial crystalline anisotropy, the domain magnetization direction follows the crystalline anisotropy axis, which is also the preferential axis of magnetization (i.e., the magnetic easy axis). Therefore, our approach to establishing a training dataset and

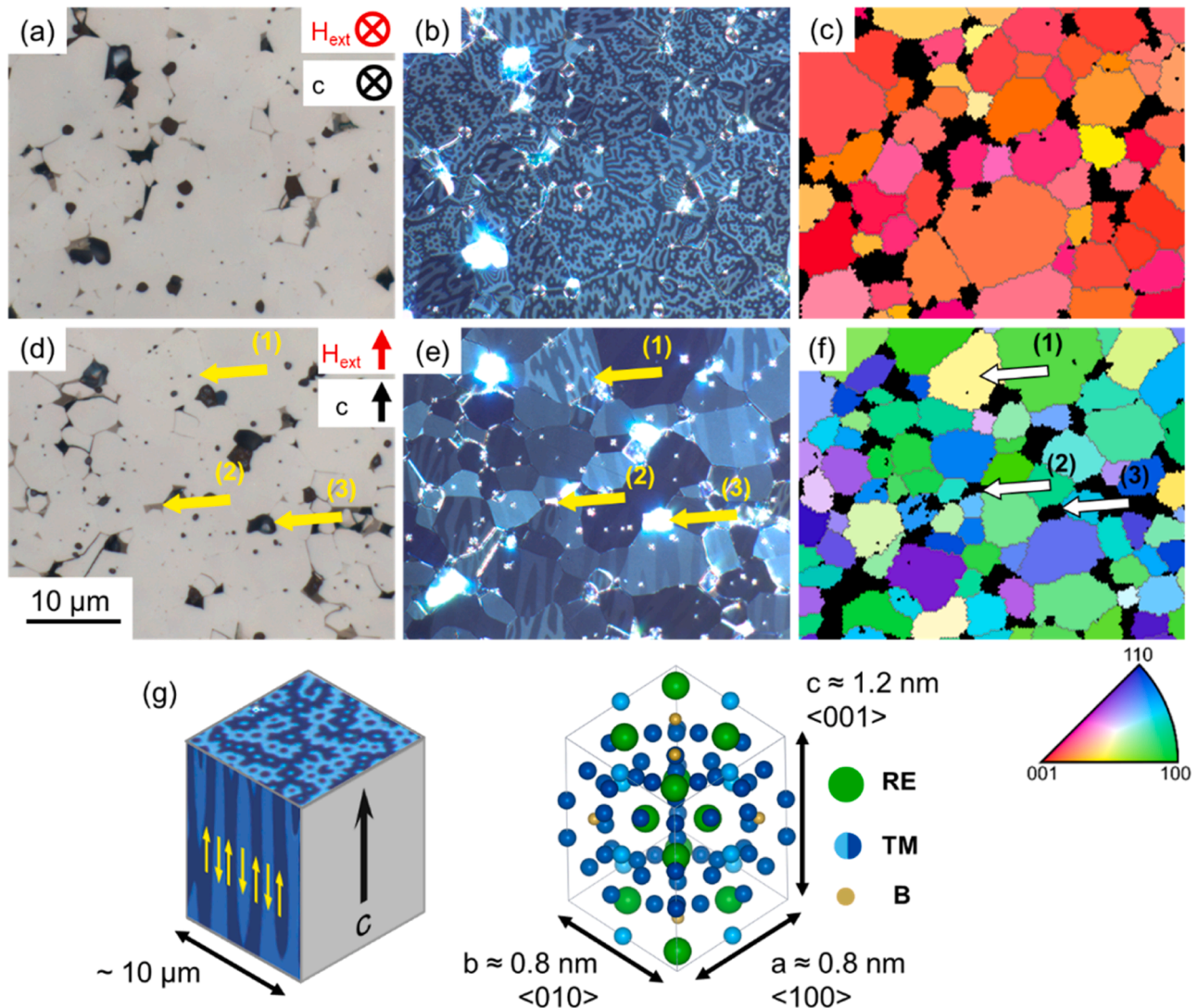
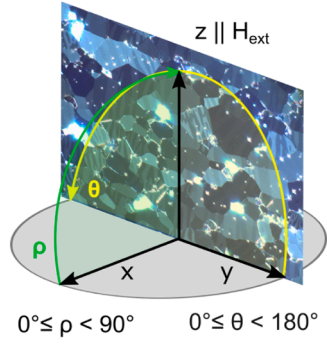


Fig. 2. Correlative microscopy of the microstructure of a sintered FeNdB-type magnet with the axis of anisotropy (c-axis) perpendicular to the image plane (a, b, c) and within the image plane (d, e, f). The bright field images (a, d) visualize (1) the hard-magnetic phase, (2) the grain boundary phase, and (3) RE-oxides and pores. In the KM images (b, e), the domain structures and the underlying grain orientation of the hard-magnetic phase become visible. The morphology of the domain patterns can be correlated with the color-coded SEM-EBSD IPF map (c, f). The morphology of the domain pattern depends on which crystallographic axis of the FeNdB-crystal structure is visible in the plane of observation (g).



**Fig. 3.** DoPACOM coordinate system for orientation quantification from Kerr microscopy image. The orientation of the grains around the x axis affects the  $\theta$  value, and their orientation around the z axis affects the  $\rho$  value.

subsequently quantifying the grain orientation distribution is based on, and limited by, the resulting polar MOKE phenomena and can be summarized as *Domain Pattern Analysis and Crystallographic Orientation Measurement (DoPACOM)*.

Grain orientation can be represented as a function of Euler angles  $\varphi_1$ ,  $\Phi$ ,  $\varphi_2$  (Bunge notation) as follows:

$$f(g) = f(\varphi_1, \Phi, \varphi_2) \quad (1)$$

The DoPACOM models were trained on orientation angles  $\theta$   $[0^\circ, 180^\circ]$  and  $\rho$   $[0^\circ, 90^\circ]$ , which are reduced forms of EBSD Euler angles  $\varphi_1$  and  $\Phi$ . A rotation corresponding to the  $\varphi_2$  angle is not detectable by polar MOKE as it was seen that for  $\varphi_2$  angle, the grains from KM did not show any visible or measurable changes nor affected the magnetic properties. Additionally, due to the symmetry, the range of Euler angles (Bunge notation) is reduced as follows:

$$\theta = \begin{cases} \varphi_1, & \text{if } \varphi_1 \geq 0^\circ \text{ and } \varphi_1 \leq 180^\circ \\ \varphi_1 - 180^\circ, & \text{if } \varphi_1 > 180^\circ \end{cases} \quad (2)$$

$$\rho = \begin{cases} \Phi, & \text{if } \Phi \geq 0^\circ \text{ and } \Phi \leq 90^\circ \\ 90^\circ - (\Phi - 90^\circ), & \text{if } \Phi > 90^\circ \end{cases} \quad (3)$$

**Fig. 3** shows the coordinate system for quantifying the reduced orientation from the Kerr microscopy image where the orientation of the grains around the x and y axis affects the orientation values  $\theta$  and  $\rho$ , respectively.

Further, in acquiring the EBSD mapping and Kerr microscopy images for the training dataset, special care had to be taken to establish the proper relative position and to ensure that the coordinate systems of the sample and the respective microscope were aligned correctly. As discussed in [Section 1.1](#), the anisotropy or alignment of the grains in the sample affects the magnet's properties, which can be controlled during the manufacturing process. [Eq. \(4\)](#) estimates the remanence of the magnet based on the degree of alignment and other parameters (non-varying) [28].

$$B_r \propto (J_s * \beta) * \left\{ \left( \frac{\rho}{\rho_0} \right) * (1 - \alpha) \right\} * f \quad (4)$$

**Table 1**

Overview of the characteristics of the sintered FeNdB magnets used for the training, validating, and testing of the machine learning models. Samples FeNdB-T and FeNdB-V were used to train and validate the models, and FeNdB-AP, FeNdB-TP, and FeNdB-IP samples were used for testing the trained model. ECD [ $\mu\text{m}$ ]  $\Phi$  is the equivalent circle diameter of the extracted grains in the sample.

Sample	Measured mean ECD $\Phi$ [ $\mu\text{m}$ ]	$B_r$ [T]	$BH_{\text{max}}$ [ $\text{kJ}/\text{m}^3$ ]	$H_{cJ}$ [ $\text{kA}/\text{m}$ ]	#Grains	Dataset
FeNdB-T	10	1.11	235	2625	3453	Training set
FeNdB-V	10	1.11	235	2625	864	Validation set
FeNdB-AP	10	1.34	340	1115	732	Test set
FeNdB-TP	10	1.41	385	1115	690	Test set
FeNdB-IP	10	1.44	400	1115	837	Test set

Where  $J_s$  is the saturation magnetization of the grains,  $\beta$  is the temperature coefficient of the saturated magnetization,  $\rho/\rho_0$  is the ratio of the actual to the theoretical density of the magnet,  $(1 - \alpha)$  is the volume fraction of the hard-magnetic FeNdB phase, and  $f$  is the fraction of the grains aligned in the direction of easy magnetization. Except for the parameter  $f$ , other parameters remain unchanged during the compaction stage of the sample manufacturing. Therefore, it can be a potential indicator for measuring the degree of grain alignment. Using our model, the grain alignment is measured in terms of the two orientation angles mentioned above, theta and rho.

## 4. Model training and architecture

### 4.1. Materials and training dataset

The training dataset was acquired by correlating the orientation data measured by SEM-EBSD-mappings with images taken using a Kerr microscope for each individual grain in the mapping area. The KM images were acquired using a Zeiss AxioImager.M2 microscope with an exposure time of 6 s at 1000x optical magnification. The microscope was set-up for polar Kerr effect with  $88^\circ$  angle between the polarization planes using a Zeiss HXP 120 C as light source. The corresponding EBSD map was acquired using a Zeiss Sigma 300 VP scanning electron microscope, operated at 20 kV and equipped with Hikari Super EBSD camera.

The acquisition time for the EBSD mappings was about 2.5 h, providing a mapping area of about  $500 \mu\text{m} \times 400 \mu\text{m}$  at  $0.7 \mu\text{m}$  step size and at a magnification of 450x. Adding 30 min post-processing time, gives 3 h until data is available. The acquisition time for the KM images in our setup was about 6 s per image. To cover the same area as in the EBSD mapping  $4 \times 4$  image tiles need to be acquired. The total acquisition time on the Kerr microscope was 20 min for 16 image tiles, including the movement of the microscope x-y-table and the adjustment of the optical focal plane for each tile.

The Euler angles from EBSD mapping are three continuous values ( $\varphi_1$ ,  $\Phi$ ,  $\varphi_2$ ) that represent the crystal orientation of each grain in the sample, and these angles are assigned to corresponding grains in the KM images. Therefore, EBSD Euler angles are considered the reference (ground truth) for training, validating, and testing the model. The samples (see [Table 1](#)) for acquiring the training dataset were micro-sections of commercially available FeNdB sintered permanent magnets, which were thermally demagnetized beforehand.

[Table 1](#) shows the overview of the samples used for experiments in this paper, their magnetic properties, and grain statistics, including the number of grains and equivalent circle diameter (ECD)  $\Phi$ . Samples FeNdB-T and FeNdB-V are used for the training and validation of the model, respectively, and samples FeNdB-AP, FeNdB-TP, and FeNdB-IP are used for testing the performance of the trained model.

FeNdB-T and FeNdB-V are axially pressed samples with a mean grain size of  $10 \mu\text{m}$  measured as an equivalent circle diameter. The sample is anisotropic and therefore has been sectioned carefully in steps of  $15^\circ$  to produce an unbiased dataset, as seen in [Fig. 4\(b\)](#). [Fig. 4\(c\)](#) shows an example of the 3D domain structure in the grain. The difference in the appearance of the domain structure is visible when it is sectioned along the surface plane and perpendicular to the surface plane. The domain

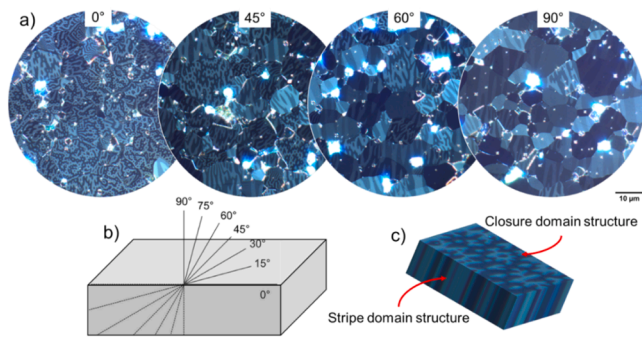


**Fig. 4.** Sample preparation for the training dataset. (a) Kerr microscopic image of a cuboid sample of the anisotropic sintered FeNdB magnets sectioned at 0°, 45°, 60°, and 90° at 1000x. The change in the appearance of the micromagnetic domain patterns when sectioned at various angles is visible. (b) The sample is sectioned in steps of 15° (c) Simulation of the domain structure appearance in 3D. The domain structure changes along the grain in 3D from closure to stripe and vice versa depending on the magnetic field direction and processing conditions or parameters.

structure patterns change from closure to stripe as the sectioned angle changes from 0° to 90°. The domain structure patterns and their contrast depend on the processing parameters and applied magnetic field. Further, the difference in the KM image of the same sample at a different sectioned angle is shown in Fig. 4.

The test samples FeNdB-AP, FeNdB-TP, and FeNdB-IP are sintered FeNdB magnets with different degrees of alignment, in which the orientation of the pressing direction to the direction of the applied external magnetic field was varied during pressing.

#### 4.1.1. Dataset for training the regression models

With the change in the orientation  $\varphi_1$  and  $\Phi$ , the image features such as domain contrast, the domain structure orientation, and the entropy of grains extracted from KM also change. However, a rotation corresponding to the  $\varphi_2$  angle is neither detectable by polar MOKE nor affects the magnetic properties. Moreover, the KM image of the magnet does not show visible changes when there are changes in the  $\varphi_2$  value. Therefore, as mentioned in Section 3, the reduced EBSD Euler angles  $\varphi_1$  and  $\Phi$  is considered for training the models.

Fig. 5 shows the distribution of 11 out of 13 Haralick parameters (HP) [29] calculated from each grain in the sample for the  $\varphi_1$  orientation values. The features extracted from grain with  $\varphi_1$  [181°, 360°] follow the same distribution as for the  $\varphi_1$  [0°, 180°]. Further, similar distribution was seen when other image features, such as the deep features

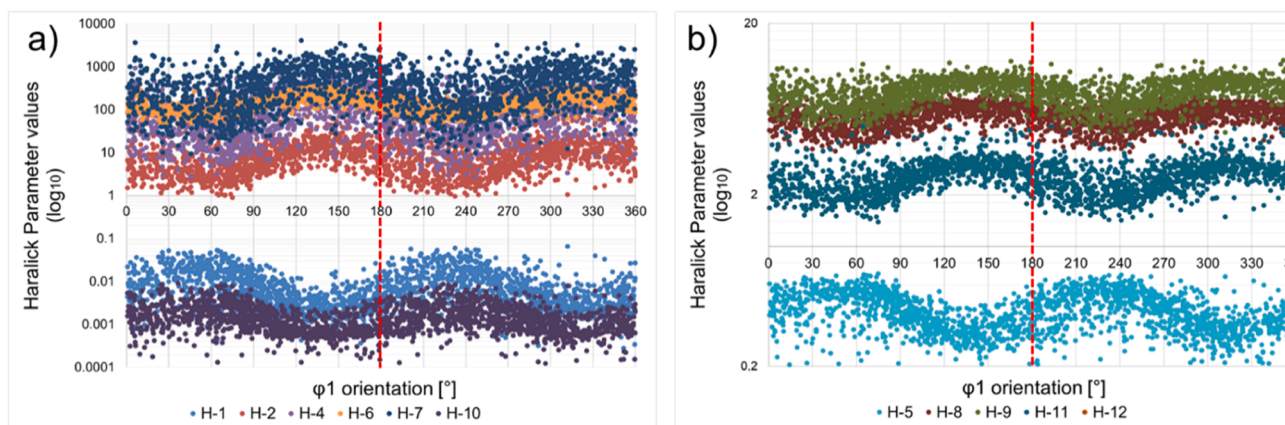


**Fig. 5.** The distribution of the texture features extracted from the individual grain image from the sample used for training the models against the  $\varphi_1$  orientation obtained from the EBSD measurement. (a) and (b) show the similarity in the features extracted from the grains with  $\varphi_1$  orientation between selected Haralick parameters against  $\varphi_1$  orientation [0°, 180°] and [181°, 360°].

from the pre-trained VGG16 model [30] and color features [31] (colorfulness and domain contrast), were extracted from the grains, suggesting that there is symmetrical behavior between  $\varphi_1$  [0°, 180°] and  $\varphi_1$  [181°, 360°]. For the  $\Phi$  orientation, the values are [0°, 95°]. Therefore, a new coordinate system was adopted with reduced  $\varphi_1$  and  $\Phi$  orientations, referred to as  $\theta$  [0°, 180°] and  $\rho$  [0°, 90°], respectively, using Eqs. (2) and (3). Haralick parameters H-1, H-2, H-4, H-6, H-7, and H-10 refer to the angular second moment, contrast, sum of squares-variance, sum average, sum variance, and difference variance, respectively [29]. And H-5, H-8, H-9, H-11, and H-12 refer to inverse difference moment, sum entropy, entropy, information measure of collection 1, and information measure of collection 2, respectively [29].

Finally, the dataset for training and testing the crystal orientation prediction model from the KM image has the extracted grains from KM as its input and corresponding  $\theta$  and  $\rho$  as the ground truth. Out of 4317 grains extracted from the FeNdB sample, 3453 grains are used for training purpose and remaining 864 grains are used for validation of the learning models. Grains from AP, TP, and IP samples are used for testing the trained models. Fig. 6 shows the distribution of grain orientation values for training the models, and it can be seen that the dataset is imbalanced, with most of the grains having  $\theta$  values in the range of 40° to 130° and  $\rho$  values greater than 30°. The dataset imbalance has been compensated using data augmentation on the grains that are less in number. Data augmentation techniques, such as adding noise and translational shifts, have been used to populate the under-sampled regions in the dataset. The augmentation involves adjusting the dimensions of the grain images, introducing a 10% shift in height and width. Furthermore, the images undergo zooming and panning operations within limits of 0.75 to 1, effectively changing their scale. Gaussian noise is added to increase the variability, ranging from 5% to 7% intensity, simulating real-world image imperfections. The application of motion blur using a kernel size of 3 contributes to this by emulating the blurring effects of motion during image capture [32]. The choice of binning size for  $\theta$  and  $\rho$ , set at 10° and 5° respectively is for the visualization only, aligns with the predetermined grain orientation tolerance values of 10° and 5° for each parameter.

#### 4.2. Grain orientation prediction models from Kerr microscopy

The models to predict the orientation of the grain from FeNdB magnet samples are regression models based on the supervised learning approach. Two separate regression models were trained to predict  $\theta$  and  $\rho$ , respectively. Traditional machine learning and advanced deep learning approaches were considered for training the orientation prediction model. The traditional ML approach includes manual feature

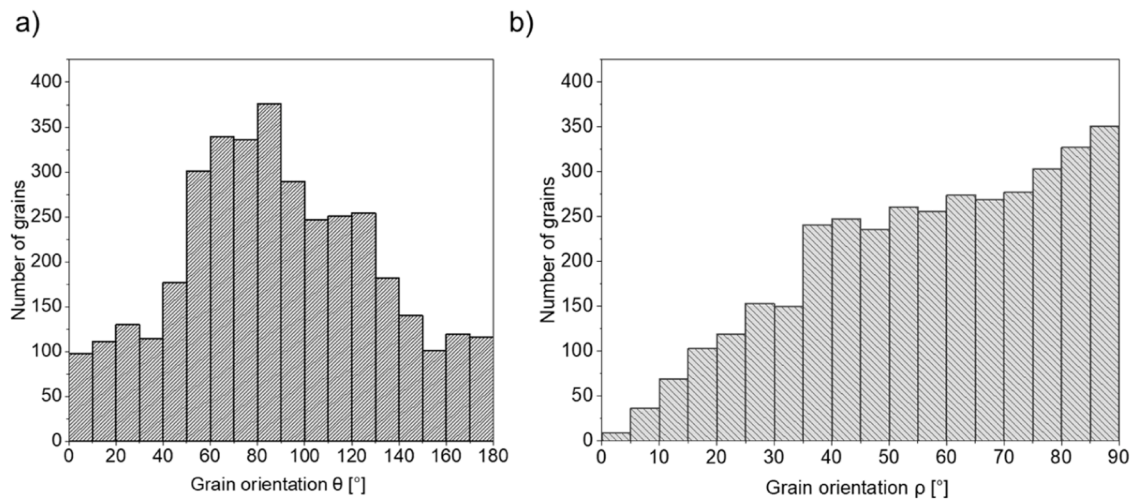


**Fig. 6.** Grain orientation data distribution used for training the ML models. (a) theta ( $\theta$ ) values and (b) rho ( $\rho$ ) values. The data distribution for the  $\theta$  and  $\rho$  predicting models are different and are processed separately. The choice of binning size here is for the visualization only.

extraction from input image data that can be used for ML model training. DL architectures are complex and feature automatic extraction from the input dataset. The KM images of FeNdB-T and FeNdB-V are preprocessed to remove the artefacts and oxides, then detecting the grain boundaries to extract the individual grains from the KM image dataset. The preprocessing steps to create a gallery of individual grain images from KM data are based on the deep learning segmentation model discussed by Choudhary et al. in [33]. As part of the post-processing steps, the grains with ECD smaller than 2  $\mu\text{m}$  are ignored. The preprocessing and post-processing steps for both ML and DL approaches remain the same. Further, the concordance coefficient of correlation [34] ( $R_{ccc}$ ), and mean absolute error (MAE) are the metric used for the comparison of ML and DL models.

$$R_{ccc} = \frac{2 * \sigma_{12}}{(\mu_1 - \mu_2)^2 + \sigma_1^2 + \sigma_2^2} \quad (5)$$

Where  $(\mu_1, \sigma_1)$  and  $(\mu_2, \sigma_2)$  are the mean and standard deviation of actual and predicted values,  $\sigma_{12}$  is the covariance for the actual and predicted values.

All the experiments were performed using Python version 3.7 and open-source libraries such as Scikit-learn for ML [35], and Keras [36], for DL, on a system with a 256 GB NVIDIA Quadro RTX 8000 graphics card.

#### 4.2.1. Traditional machine learning regression model

Different features from grains are extracted manually to train the ML model to predict  $\theta$  and  $\rho$  from the grains of KM data. Table 2 shows the different features extracted from each grain in the samples, including texture, color, shape, morphology, and domain statistics information. The size of the feature set is 45-dimensional, with 13 Haralick parameters describing the textural information in the grain. There are three morphological features, three domain network statistics, one RGB colorfulness [31], and 25 features from Zernike moments [37] that

**Table 2**

Types of features extracted manually from each grain in the sample and description of the parameters extracted from each feature.

Features	Description
Texture	Haralick parameters
Color	RGB colorfulness
Shape	Zernike moments
Morphology	Orientation, aspect ratio, and area
Domain Statistics	Nodes, longest pattern, and standard deviation between patterns

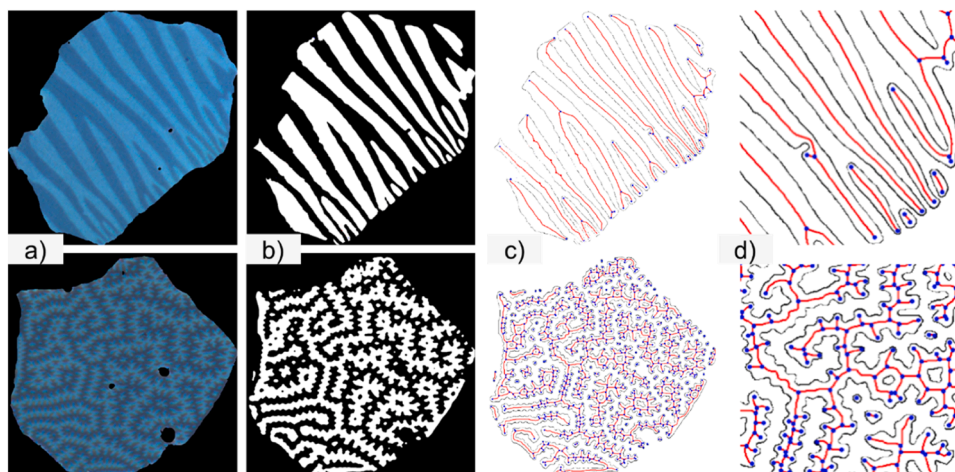
provide information to characterize and quantify the shape of the domain structures. The domain structure's mean orientation, aspect ratio, and grain area are the three morphological features. The remaining three features are domain statistics calculated from the skeletonized image of domain structures [38].

Fig. 7 shows examples of the skeletonized image of the domain structure, which is used to calculate statistics such as the number of nodes, longest pattern, and standard deviation between the individual domain patterns within the grain. Fig. 7(c) and (d) show the nodes in the blue dots and the skeleton of the pattern referred to as branches in red. The grains with stripe patterns have a lesser number of nodes and branches. Further, the branches for the grains with stripe patterns are more sparsely distributed than in grains with the closure domain patterns, as seen in Fig. 7(c).

The extracted 45-dimensional feature is used to train different traditional regression models that include tree-based models such as AdaBoost regressor with the random forest as a base learner (A-RF), gradient boosting (GB), and extreme gradient boosting (XGB) as well as simple artificial neural networks such as a multi-layer perceptron (MLP). Based on the model's performance on the validation dataset, hyper-parameters were tuned for better generalization and to avoid overfitting.

#### 4.2.2. Advanced deep learning regression model

The limited data for training a DL model imposes constraints, as it becomes challenging to converge the model to learn meaningful information from the dataset. Therefore the transfer learning [39] approach has been considered, which has the advantage of generalizing well to the custom dataset of a smaller size despite its being trained on different subjective knowledge (e.g., ImageNet [40] and CIFAR-100 [41]). The transfer learning technique has frozen the pre-trained model's feature extraction layer. The custom fully connected (FC) layers replace the existing FC layer to adapt the domain orientation datasets. The feature extraction layers from different pre-trained models were tested alongside the custom FC layer. Pre-trained models such as VGG16 [30], ResNet50V2 [42], and EfficientNetB0 [43] are screened out of different pre-trained models that are trained on ImageNet [31]. Since these pre-trained models are trained on the classification task, the final layers are replaced by the custom FC layers with a regression layer to output continuous values instead of discrete values. The custom FC layer has three dense layers with 32, 16, and 8 neurons in each layer, respectively, with batch normalization with weight decay of 0.001 and momentum set to 0.9, dropout layer with 60% dropout rate, and L2 regularization with  $1 \times 10^{-4}$  as decay or lambda value to avoid overfitting the learning models. The dense layers have ReLu as activation function and weights



**Fig. 7.** Workflow to extract the domain structures and calculate domain statistics from different grains. (a) original images of grains, (b) binary mask of the extracted domain structures, (c) domain network, and (d) domain network showing nodes in blue and branches in red, respectively. (For interpretation of the references to colour in this figure legend, the reader is referred to the web version of this article.)

are initialized with Xavier initialization [44]. Additionally, a simple baseline convolutional neural network (CNN) with four convolutional layers, two 2D max-pooling layers, and three dense layers with a final layer having one output was trained alongside pre-trained models. This baseline model was considered to form a basis for expectations from the pre-trained model with better feature extraction layers.

The input image for all DL regression models is an RGB image of  $224 \times 224$  pixels. Mean squared error and mean absolute percentage error was used as the loss function and performance metrics, respectively, using Adam as the optimizer with a dynamic learning rate. The reduce on plateau [45] approach was chosen to reduce the learning rate by 0.1 when the model stops learning for ten continuous epochs, with the minimum learning rate being  $1 \times 10^{-9}$ . The batch size is set to 24. The model's hyperparameters to predict  $\theta$  and  $\rho$  are the same, and models were trained for 500 and 300 epochs, respectively.

## 5. Results

### 5.1. Performance evaluation of the grain orientation predicting model

The performance evaluation on the validation dataset with 864 grains from the FeNdB-V sample was compared for the trained ML and DL models. Among the traditional ML models considered for the experiments, the A-RF model achieved the highest performance for both  $\theta$  and  $\rho$  in terms of the MAE and  $R_{ccc}$ . The MAE for  $\theta$  and  $\rho$  from the trained A-RF model are  $7.0^\circ$  and  $5.0^\circ$  respectively. Similarly, the  $R_{ccc}$  for  $\theta$  and  $\rho$  are 0.84 and 0.81 respectively. Conversely, the fine-tuned EfficientNetB0 model achieved the lowest MAE value for both  $\theta$  and  $\rho$ , of

**Table 3**

Performance comparison among different machine learning and deep learning regression models tested on the validation set for prediction of grain orientations. The fine-tuned EfficientNetB0 outperformed in terms of the mean absolute error (MAE) and correlation coefficient ( $R_{ccc}$ ).

Models	$\theta$ [ $^\circ$ ]		$\rho$ [ $^\circ$ ]	
	MAE	$R_{ccc}$	MAE	$R_{ccc}$
ML				
A-RF	7.0	0.84	5.0	0.81
GB	8.7	0.64	8.3	0.76
XGB	9.2	0.73	5.1	0.80
MLP	11.4	0.56	10.3	0.59
DL				
Baseline model	9.6	0.61	9.1	0.67
VGG16 fine-tuned	6.9	0.86	5.7	0.84
ResNet50V2 fine-tuned	6.6	0.88	4.9	0.89
EfficientNetB0 fine-tuned	3.5	0.93	3.0	0.94

$3.5^\circ$  and  $3.0^\circ$  respectively, among all the models.

Table 3 shows the performance of each ML and DL model for the validation set. The baseline model predicted the  $\theta$  and  $\rho$  values with a higher error than the other DL models.

Fig. 8(a-d) compares the trained A-RF model and fine-tuned EfficientNetB0 model on the validation dataset. The predictions from the A-RF model on grains with  $\theta$  values lower than  $60^\circ$  and higher than  $120^\circ$  produced a very high error when compared to the grains with  $\theta$  values in the range of  $60^\circ$  to  $120^\circ$ . That would mean the A-RF model fails to learn the accurate data distribution and only performs well on grains with  $\theta$  values in the  $60^\circ$  to  $120^\circ$  range. However, the fine-tuned EfficientNetB0 model predicts the orientation with high error for grains with  $\theta$  values less than  $10^\circ$  and more than  $170^\circ$ .

The difference in the performance of the trained models on the validation set for the  $\rho$  prediction can be seen in Fig. 8(c) and (d). The A-RF model results in more variance, with a MAE of  $5.0^\circ$  and  $R_{ccc}$  of 0.81 compared to the fine-tuned EfficientNetB0 model, which predicts with lesser error and agrees well with measured EBSD values. The fine-tuned EfficientNetB0 has a MAE of  $3.0^\circ$  and  $R_{ccc}$  of 0.94. Out of the 8 different regression models trained, fine-tuned EfficientNetB0 model resulted in lowest prediction error for both  $\theta$  and  $\rho$  as shown in Table 3. The generalization ability of trained model is primarily assessed on the test set. The grains from the test samples FeNdB-AP, FeNdB-TP and FeNdB-IP also referred as AP, TP and IP respectively are not part of training and validation set. Fig. 8 (e-f) shows performance of the fine-tuned EfficientNetB0 model on test set samples which resulted in the MAE less than 5.0 for both  $\theta$  and  $\rho$  values.

### 5.2. Measuring the robustness of the trained DL model on samples with different degrees of alignment

From the above discussion, it can be concluded that the trained DL model (fine-tuned EfficientNetB0) outperforms the traditional ML model (A-RF) in predicting grain orientation from the KM data for the magnet samples. One of the applications of the trained crystal orientation prediction model could be to determine the grain alignment in the samples, which is affected by the processing conditions of the sintered magnet samples, affecting extrinsic magnetic properties such as remanence ( $B_r$ ).

As discussed in Section 1.1, the manufacturing process affects the alignment of the grains and accordingly produces AP, TP, or IP samples. AP, TP, and IP samples are considered in evaluating model performance for new samples not part of the training and validation set.

As shown in Fig. 9, the IP samples have grains with domain patterns that are better aligned in one direction and achieve higher  $B_r$  than the AP

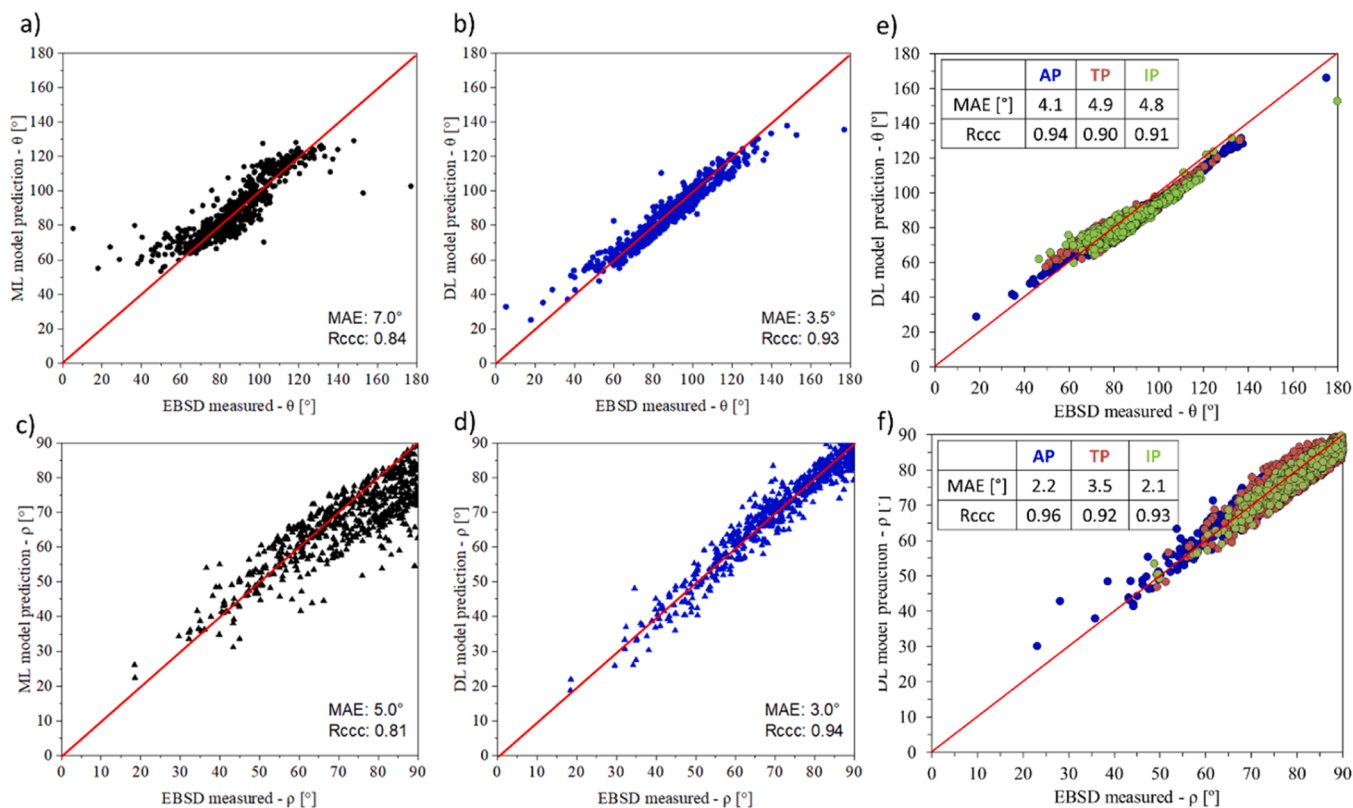


**Fig. 8.** Comparison between the predictions from trained ML (adaptive boosted random forest) and fine-tuned DL (EfficientNetB0) regression models against the ground truth EBSD measurements on the validation set. (a) theta predictions from the ML model, (b) theta ( $\theta$ ) predictions from the DL model, (c) rho ( $\rho$ ) predictions from the ML model, and (d) rho ( $\rho$ ) predictions from the DL model. Additionally, the performance of the fine-tuned DL regression model on test set for predicting (e) theta and (f) rho is shown.

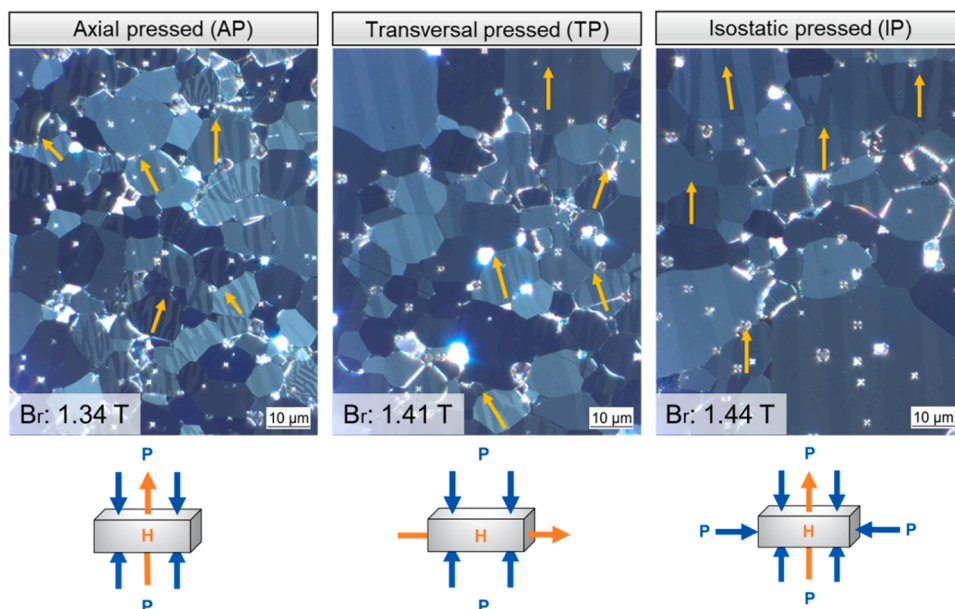


**Fig. 9.** Kerr micrographs showing the grain orientation of the axially pressed (AP), transversal pressed (TP), and isostatically pressed (IP) sintered FeNdB magnet at 1000x magnification. The measured magnetic remanence ( $B_r$ ) increases from AP to IP. The schematic diagram shows the AP, TP, and IP samples' pressing ( $P$ ) and magnetic field ( $H$ ) direction. Ideally, a uniaxial grain orientation distribution (texture) along the indicated direction of  $H_{ext}$  is produced.

and TP samples. TP has better  $B_r$  than AP samples because of the higher number of grains aligned along the geometric axis of preferential orientation. This information can be obtained from the grain orientation, and the sample with lesser spread or standard deviation for grain

orientation ( $\theta$  and  $\rho$ ) values within the sample has better grain alignment, suggesting that the sample has high remanence and a high degree of alignment.

Moreover, one of the ways to evaluate the statistical reliability of the

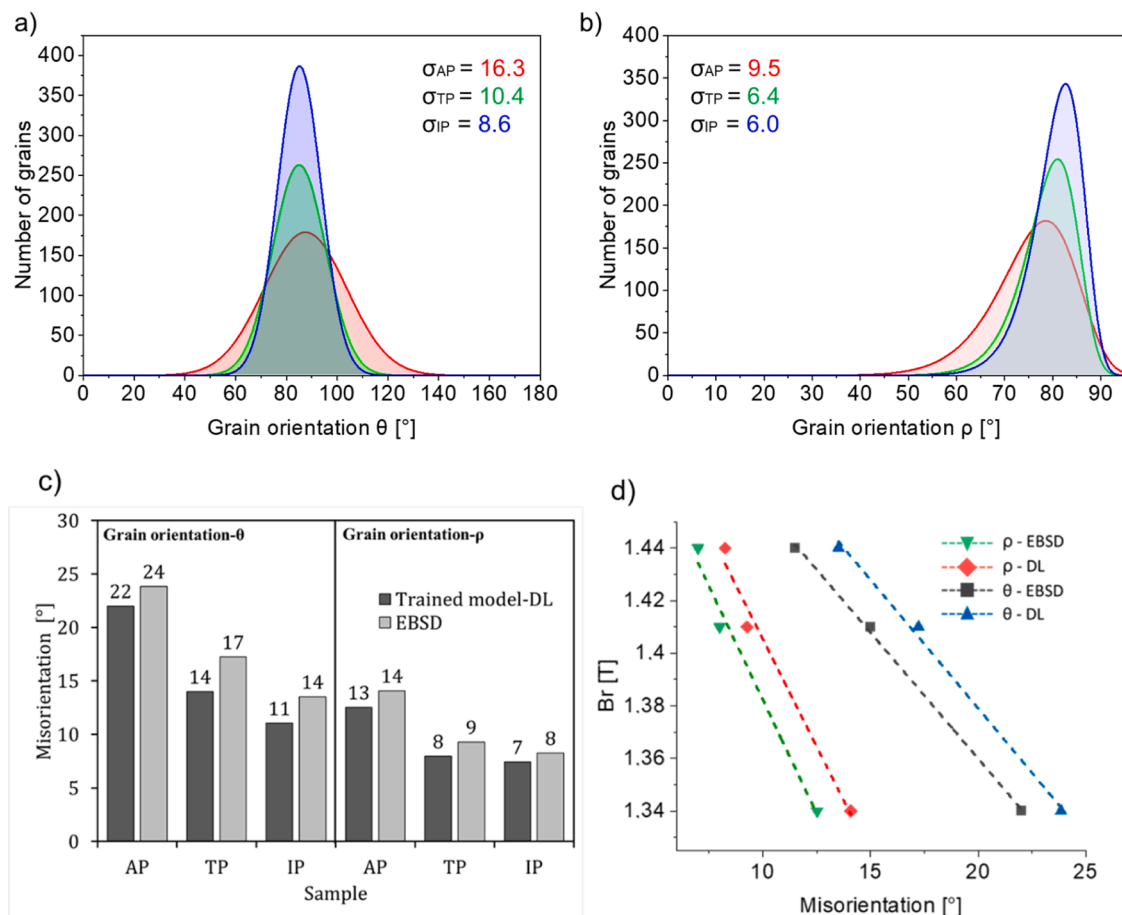


**Fig. 10.** Statistical reliability of the predictions from the fine-tuned DL regression model found by correlating them with magnetic remanence ( $B_r$ ) of the samples with different degrees of alignment or texture. (a) and (b) histogram of the predicted theta and rho orientation from grains of AP, TP, and IP samples showing the spread of the dataset as a standard deviation, (c) calculated misorientation as a function of interquartile range from histogram orientation (deviation from axis of easy magnetization) of theta and rho obtained from trained model predictions and EBSD respectively, and (d) linear correlation between the  $B_r$  and misorientation in AP, TP and IP samples obtained from predicted values and measured EBSD.

DL-based predictions is to correlate the predicted orientation of grains in each sample with the intrinsic magnetic property, such as magnetic remanence. Sawatzki et al. [46] calculated the remanence values of FeNdB sintered magnets by using the orientation histogram from EBSD to demonstrate the reliability of the orientation histogram with magnetic measurements. The statistical dispersion of the grain orientation of each sample can be measured using different methods, such as standard deviation (SD) or interquartile range (IQR). The predicted grain orientation distribution in the AP, TP, and IP samples in terms of the  $\theta$  values are non-skewed with Gaussian curve fitting. However, for the  $\rho$  values, there is a skewed right-hand distribution, and Weibull curve fit is selected, as seen in Fig. 10 (a and b). The spread of the data distribution can be statistically linked to grain misorientation. For this, the deviation of each grain's orientation from the axis of easy magnetization for all grains in the sample is calculated. Misorientation is then quantified using the IQR as a measure of data spread, providing insight into the overall variability in grain orientation values relative to the axis of easy magnetization.

Further, Fig. 10(c) and 10(d) show that there is a similar trend between the magnetic remanence ( $B_r$ ) and misorientation values obtained from the orientation histogram of the  $\theta$  and  $\rho$  using the EBSD and trained DL method. The magnetic remanence for the AP sample is lower than in TP and IP samples, and it is due to the fact that there is high misorientation in grains from the AP sample than in TP and IP, which can also be seen from the results of the predicted values from the trained DL model (shown in Fig. 10(c)). In Fig. 10(d), for each of the four lines, three

misorientation points represent AP, TP and IP samples respectively. The points with the highest  $B_r$  value of 1.44 T is IP, and the lowest  $B_r$  value of 1.34 T is the AP sample. The one with a  $B_r$  value of 1.41 T is the TP sample.

## 6. Discussion

One of the preprocessing steps for the grain orientation prediction workflow involves extracting the grains from KM images via a pre-trained grain extraction model using the approach described in [33]. It requires the removal of artefacts such as pores and oxides, followed by the trained grain boundary detection model to extract individual grains. During the post-processing steps to clean the raw EBSD map, the morphology of the grains changes [47] such that the pores and oxides inside the grains are filled with the nearest pixels. Fig. 11 shows that pores are replaced with neighboring pixels for the grains marked as 1 and 2. Further, the morphology of the grains is also influenced by the applied post-processing step in EBSD [47]. However, further investigation of the grain size comparison between the results from KM (trained models) and EBSD suggests that the Kerr micrographs provide flexibility to carry out precise grain size analysis by eliminating the after effects of post-processing step carried out as part of EBSD.

Nevertheless, using the KM image for the grain size analysis approach offers more flexibility in that the measurement of grain structure can be carried out via two methods. The Kerr microscopy approach (A) involves measuring the grain with actual internal

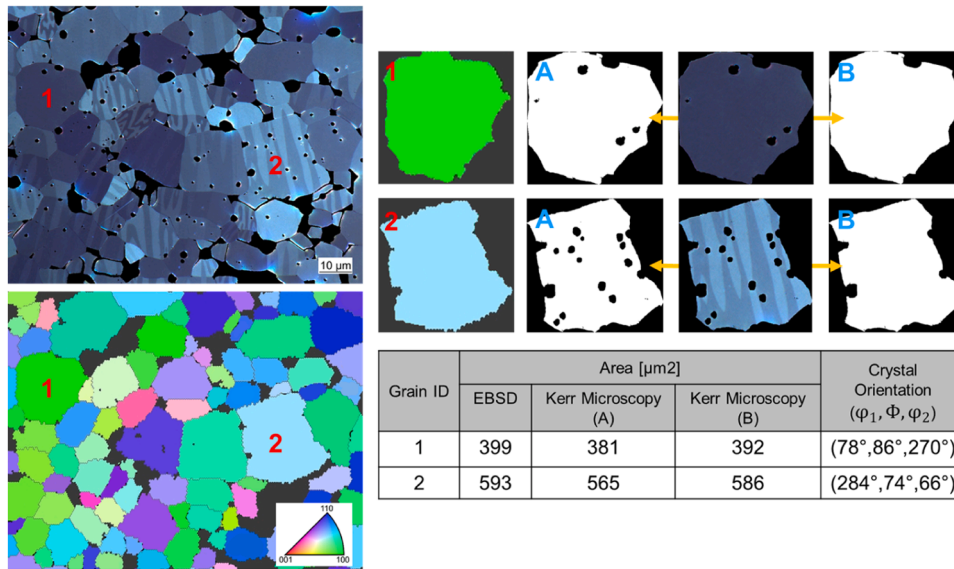


**Fig. 11.** Correlative Kerr micrograph and SEM-EBSD map of sintered FeNdB magnet, showing the difference in the area of the two specific grains using a measured EBSD approach and the calculated area from KM using approaches (A) and (B). Approach (B) fills holes caused by pores and oxides with neighboring pixels, resulting in an area close to measured EBSD values. Approach (A) results in a lower grain area as holes are left as it is.

structures, so pores and oxides are not included. Kerr microscopy (B) involves filling the regions containing pores and oxides within the grains with the nearest pixels and bringing them closer to the EBSD measurements. The grain size measured using all three approaches is shown in Fig. 11, and the difference in results is due to the change in the morphology of grains in the EBSD map. This highlights the importance of Kerr microscopy for sample characterization involving grains, as it provides information that is close to reality.

However, note that for the grain orientation prediction models the correlative KM and SEM-EBSD data are needed for training phase only. Once the models are trained, only KM images of the test samples are needed as the input to predict the grain orientations.

### 6.1. Performance comparison between ML and DL approaches

The random forest regressor with adaptive boosting gives better results than the other traditional ML approaches tested. Compared to the ensemble or tree-based models (A-RF, GB, and XGB), MLP, an artificial neural network, struggled with structured data due to its preference for unstructured data like images [48]. Moreover, XGB has proven to optimize better than GB and RF when tested on tabular data. However, due to the size of the training set here, it was more feasible to tune the A-RF model compared to XGB, which involves highly sensitive hyperparameter tuning.

The performance of the A-RF model suggests that the features extracted from the grains have a definite relationship with the ground truth values of  $\theta$  and  $\rho$ . The feature importance plot suggests that texture, color, morphology, and domain statistics notably affected model generalization, while shape features had minimal impact and can be omitted in future A-RF training.

However, fine-tuned DL models outperformed ML models. The baseline DL model, with only fully connected layers, struggled to generalize from the training dataset. The baseline's prediction error was about 2.5 times higher than EfficientNetB0 and nearly twice as high as fine-tuned VGG16 and ResNet50V2 models. This underscores the significance of transfer learning, suggesting that direct training on the FeNdB-T magnet grain dataset couldn't adequately learn the correlation between grain features and orientation. Pre-trained models excel at feature extraction, even though they are trained on different subjective knowledge, such as the ImageNet dataset [49].

The high error of the fine-tuned EfficientNetB0 model in predicting  $\theta$  values for grains with  $\theta < 10^\circ$  or  $> 170^\circ$  could stem from the limited training examples in that range, as noted in Section 4.1. For  $\rho$  prediction, the trained A-RF model struggled with grains having  $\rho > 70^\circ$ , despite a substantial number of training grains falling between  $60^\circ$  and  $90^\circ$   $\rho$  values significantly impact grain domain contrast [50], particularly for higher  $\rho$  values due to diminished contrast. The A-RF model couldn't generalize over the skewed dataset distribution (seen in Fig. 6(b)) due to the lack of adequate features explaining domain contrast variation. In contrast, the fine-tuned EfficientNetB0 model exhibited better generalization, underscoring the DL approach's auto feature extraction capturing diverse image features.

### 6.2. Evaluation of robustness of the trained DL model on samples with different degrees of alignment

The plots for AP, TP, and IP samples in Fig. 10(c) exhibit strong agreement between predicted and measured EBSD values. The mean difference for  $\theta$  is under  $4^\circ$  for AP and IP, and under  $2^\circ$  for  $\rho$ , indicating a minor consistency bias in DL model predictions, approximately 2% for both  $\theta$  and  $\rho$ . The agreement limits for  $\theta$  are below  $10^\circ$ , and below  $5^\circ$  for  $\rho$ , despite the higher remanence in the testing samples compared to the training sample (Table 1).

Furthermore, the standard deviation of predicted orientation values histogram distribution in Fig. 10(a) and (b) suggests that AP has a wider spread compared to TP and IP. IP exhibits a smaller spread of  $8.6^\circ$  for  $\theta$  and  $6.0^\circ$  for  $\rho$ , indicating more grains aligned in one direction. This improvement in grain alignment from AP to IP can be attributed to sample characteristics, with IP having a Br of 1.44 T, significantly higher than AP's 1.34 T.

Moreover, as expected, the misorientation value decreased from AP to IP, closely mirroring the trend observed with the EBSD values, as shown in Fig. 10(d.) Both EBSD and the trained DL model exhibited a similar negative linear correlation between misorientation and Br. The deviation between predicted and EBSD values based on misorientation data ranged from  $1^\circ$  to  $4^\circ$ . Thus, the DL model's predicted values align well with the EBSD method for grain orientation determination.

### 6.3. Strengths and limitations

In addition to the prediction accuracy achieved with the DL model, our approach offers two important advantages compared to analyzing the anisotropy of sintered FeNdB-magnets using EBSD mappings. Firstly, the time needed for data acquisition and processing is significantly shorter with our method. Considering an area typical for single EBSD-mappings, 500  $\mu\text{m}$  x 400  $\mu\text{m}$  in our case, this takes about 3 h with EBSD but only about 20 min for KM-image acquisition and processing. The combined time required to initialize the developed model for  $\theta$  and  $\rho$  value is 8 s and to apply on the KM-image of 16 tile images (4317 grains) with 1000x magnification including the pre and post processing steps is 16 min. Thus, with our experimental setup, measurements can be provided about 5 times faster and has prediction error below 5°.

Secondly, our approach enables users of Kerr microscopes to do quantification of anisotropy of sintered FeNdB magnets without the need to use SEM-EBSD equipment, which is usually more expensive in purchase and more complex in operation than microscopes with a MOKE-functionality. Also, acquiring images over a large distance on the sample is easier on a microscope than in SEM-EBSD. This becomes a benefit when the goal is to analyze a large, coherent sample area.

Nevertheless, the developed approach has limitations to consider. The model predicts orientation comparatively less accurately and with lower confidence when the sample contains many grains with closure domain structures. These structures are common when samples are sectioned perpendicular to the applied magnetic field. To improve prediction accuracy, it's advisable to obtain samples for analysis with fewer fully developed closure domain structures. Additionally, it is to be noted that the developed approach predicts reduced Euler angles where  $\varphi_2$  orientation not included as it was observed that KM image did not have information that can be used for training the ML or DL models. Finally, the applicability of developed models in this paper is shown for RE-based sintered magnets, which account for about 20% of the permanent magnet volumetric market with annual sales of ~18 billion US\$ in 2020 [51]. In future work, we aim to demonstrate that our method of analyzing MOKE images using deep learning concepts can also be applied to SmCo-type sintered magnets.

### 7. Conclusions and further work

We present the results of a data-driven approach for the quantification of anisotropy of sintered FeNdB magnets using data from Kerr microscopy images. The use of correlative Kerr microscopy and SEM-EBSD mappings for the dataset preparation to train models is presented in this paper. The effectiveness of traditional machine learning and the advanced deep learning approach for predicting grain orientation based on the grain image obtained from KM data is discussed in detail.

The trained DL model outperforms the traditional tree-based ML model for the prediction of grain orientation and produces a low error of about 2% when compared to the EBSD approach. Further, the trained DL model provides stability and robustness when tested on samples with different degrees of alignment that were not part of the training set. The model prediction produced an error of 1°–4° for AP, TP, and IP samples. The relationship between the reliable statistics obtained from the orientation histogram and magnetic property remanence was considered in evaluating the performance of the developed DL-based approach. Furthermore, we demonstrated that using our experimental setup, the duration for data acquisition and processing of KM images by DL model for orientation prediction is reduced by a factor of 5 compared to EBSD.

Considering the growing database of grains from FeNdB magnets with different grain sizes, along with rapid developments in machine learning architecture, it should be possible to overcome the current limitations of the developed model. As part of future work, analyzing the anisotropy of sintered FeNdB magnets with non-uniform grain orientation distribution, such as with pole strength differences using the developed approach will be carried out.

Lastly, considering expanding our approach to resin-bonded FeNdB magnets and other types of hard-magnetic materials, such as SmCo-type sintered magnets, we are confident that the procedure of training models of KM images and EBSD-data is also suitable for quantifying the anisotropy in these materials.

### Supplementary Material

Refer to the supplementary material for the comparison between the predicted grain orientation values from fine-tuned DL model and measured EBSD values for the isotropic sintered FeNdB magnet. The information on the time and effort for hyper-parameter tuning of the models for grain orientation prediction are also included.

### Declaration of Competing Interest

The authors declare that they have no known competing financial interests or personal relationships that could have appeared to influence the work reported in this paper.

### Acknowledgement

The authors would like to acknowledge the support from Carl Zeiss Foundation and German Research Foundation (DFG) for funding this work under project MaKerr (Grant no: 413993866).

### Supplementary materials

Supplementary material associated with this article can be found, in the online version, at [doi:10.1016/j.actamat.2023.119563](https://doi.org/10.1016/j.actamat.2023.119563).

### References

- [1] X. Yuan, J. Zhu, Misorientations across boundary planes in a sintered NdFeB permanent magnet, *RSC Adv.* 12 (31) (2022) 20412–20422, <https://doi.org/10.1039/D2RA01670B>.
- [2] J. Cui, et al., Manufacturing processes for permanent magnets: part I—sintering and casting, *JOM* 74 (4) (2022) 1279–1295, <https://doi.org/10.1007/s11837-022-05156-9>. Apr.
- [3] R.w. Gao, D.h. Zhang, H. Li, J.c. Zhang, Effects of the degree of grain alignment on the hard magnetic properties of sintered NdFeB magnets, *Appl. Phys. A Mater. Sci. Process.* 67 (3) (1998) 353, <https://doi.org/10.1007/s003390050783>. Sep.
- [4] R. Hilzinger, W. Rodewald, *Magnetic materials: Fundamentals, Products, Properties, Applications, Publicis, Germany.*
- [5] *Advances in Nuclear Fuel Chemistry* D. Manara, et al., 2 - Experimental methods, in: M.H.A. Piro (Ed.), Woodhead Publishing Series in Energy, Woodhead Publishing, 2020, pp. 89–158, <https://doi.org/10.1016/B978-0-08-102571-0.00003-3>.
- [6] R.L. Snyder, J. Fiala, H.J. Bunge, *Defect and Microstructure Analysis by Diffraction*, Oxford University Press, 1999, p. 10.
- [7] R. Schäfer, Investigation of domains and dynamics of domain walls by the magneto-optical Kerr-effect. Handbook of Magnetism and Advanced Magnetic Materials, John Wiley & Sons, Ltd, 2007, <https://doi.org/10.1002/9780470022184.hmm310>.
- [8] J. McCord, Progress in magnetic domain observation by advanced magneto-optical microscopy, *J. Phys. D: Appl. Phys.* 48 (33) (2015), 333001, <https://doi.org/10.1088/0022-3727/48/33/333001>. Jul.
- [9] H. Tas, Orientation determinations with polarized light, *Metallography* 6 (1) (1973) 1–8, [https://doi.org/10.1016/0026-0800\(73\)90012-8](https://doi.org/10.1016/0026-0800(73)90012-8). Feb.
- [10] L. Böhme, L. Morales-Rivas, S. Diederichs, E. Kerscher, Crystal c-axis mapping of hcp metals by conventional reflected polarized light microscopy: application to untextured and textured cp-Titanium, *Mater. Charact.* 145 (2018) 573–581, <https://doi.org/10.1016/j.matchar.2018.09.024>. Nov.
- [11] M. Peterzell, F. Kohlmann, C.J.L. Wilson, C. Seiler, A.J.W. Gleadow, A new approach to crystallographic orientation measurement for apatite fission track analysis: effects of crystal morphology and implications for automation, *Chem. Geol.* 265 (3) (2009) 527–539, <https://doi.org/10.1016/j.chemgeo.2009.05.021>. Jul.
- [12] X. Wang, S. Yang, M. Seita, Combining polarized light microscopy with machine learning to map crystallographic textures on cubic metals, *Mater. Charact.* 190 (2022), 112082, <https://doi.org/10.1016/j.matchar.2022.112082>. Aug.
- [13] K.-W. Jin, M. De Graef, c-Axis orientation determination of  $\alpha$ -titanium using computational polarized light microscopy, *Mater. Charact.* 167 (2020), 110503, <https://doi.org/10.1016/j.matchar.2020.110503>. Sep.
- [14] B. Gasque, L. Hendl, X. Wang, M. Seita, Optical characterization of grain orientation in crystalline materials, *Acta Mater.* 194 (2020) 558–564, <https://doi.org/10.1016/j.actamat.2020.05.027>. Aug.

- [15] M. Seita, M.M. Nimerfro, M.J. Demkowicz, Acquisition of partial grain orientation information using optical microscopy, *Acta Mater.* 123 (2017) 70–81, <https://doi.org/10.1016/j.actamat.2016.10.021>. Jan.
- [16] K. Hara, T. Kojima, K. Kutsukake, H. Kudo, N. Usami, A machine learning-based prediction of crystal orientations for multicrystalline materials, *APL Mach. Learn.* 1 (2) (2023), 026113, <https://doi.org/10.1063/5.0138099>. May.
- [17] B. Lan, et al., Direct volumetric measurement of crystallographic texture using acoustic waves, *Acta Mater.* 159 (2018) 384–394, <https://doi.org/10.1016/j.actamat.2018.08.037>. Oct.
- [18] O. Ilchenko, et al., Fast and quantitative 2D and 3D orientation mapping using Raman microscopy, *Nat. Commun.* 10 (1) (2019) 1, <https://doi.org/10.1038/s41467-019-13504-8>. Art. no. Dec.
- [19] D.H. Hurley, S.J. Reese, F. Farzbod, Application of laser-based resonant ultrasound spectroscopy to study texture in copper, *J. Appl. Phys.* 111 (5) (2012), 053527, <https://doi.org/10.1063/1.3692386>. Mar.
- [20] R. Liu, A. Agrawal, W. Liao, A. Choudhary, and M. De Graef, 'Materials discovery: understanding polycrystals from large-scale electron patterns', in *2016 IEEE International Conference on Big Data (Big Data)*, Dec. 2016, pp. 2261–2269. doi:10.1109/BigData.2016.7840857.
- [21] Z. Ding, E. Pascal, and M.D. Graef, 'Indexing of electron back-scatter diffraction patterns using a convolutional neural network', 2020, doi:10.1016/j.actamat.2020.08.046.
- [22] Z. Ding, C. Zhu, and M.D. Graef, 'Determining crystallographic orientation via hybrid convolutional neural network', 2021, doi:10.1016/J.MATCHAR.2021.111213.
- [23] Y.-F. Shen, R. Pokharel, T.J. Nizolek, A. Kumar, T. Lookman, Convolutional neural network-based method for real-time orientation indexing of measured electron backscatter diffraction patterns, *Acta Mater.* 170 (2019) 118–131, <https://doi.org/10.1016/j.actamat.2019.03.026>. May.
- [24] D. Jha, et al., Extracting grain orientations from EBSD patterns of polycrystalline materials using convolutional neural networks, *Microsc. Microanal.* 24 (5) (2018) 497–502, <https://doi.org/10.1017/S1431927618015131>. Oct.
- [25] H.M. Fitzek et al., 'Correlative microscopy and machine learning –new tools for material characterization: 20th Plansee Seminar', 2022.
- [26] A.K. Choudhary, A. Jansche, T. Bernthaler, G. Schneider, Machine learning for microstructure quantification of different material classes, *Pract. Metallogr.* 57 (7) (2020) 475–501, <https://doi.org/10.3139/147.110632>. Jul.
- [27] M. Wittwer, M. Seita, A machine learning approach to map crystal orientation by optical microscopy, *npj Comput. Mater.* 8 (1) (2022) 8, <https://doi.org/10.1038/s41524-021-00688-1>. Dec.
- [28] Y. Kaneko, K. Kitajima, N. Takusagawa, Preparation of Sr-Ferrite Magnets by the new Annealing-Remilling process, *J. Ceram. Soc. Jpn.* 101 (1176) (1993) 905–912, <https://doi.org/10.2109/jcersj.101.905>.
- [29] R.M. Haralick, K. Shanmugam, I. Dinstein, Textural features for image classification, *IEEE Trans. Syst. Man Cybern.* 3 (6) (1973) 610–621, <https://doi.org/10.1109/TSMC.1973.4309314>. SMC-Nov.
- [30] K. Simonyan and A. Zisserman, 'Very deep convolutional networks for large-scale image recognition'. arXiv, Apr. 10, 2015. doi:10.48550/arXiv.1409.1556.
- [31] D. Hasler, S.E. Suesstrunk, Measuring colorfulness in natural images. *Human Vision and Electronic Imaging VIII*, SPIE, 2003, pp. 87–95, <https://doi.org/10.1117/12.477378>. Jun.
- [32] A. Buslaev, V.I. Iglovikov, E. Khvedchenya, A. Parinov, M. Druzhinin, A.A. Kalinin, Albumentations: fast and flexible image augmentations, *Information* 11 (2) (Feb. 2020) 2, <https://doi.org/10.3390/info11020125>. Art. no.
- [33] A.K. Choudhary, et al., Grain size analysis in permanent magnets from Kerr microscopy images using machine learning techniques, *Mater. Charact.* 186 (2022), 111790, <https://doi.org/10.1016/j.matchar.2022.111790>. Apr.
- [34] L.I.-K. Lin, A Concordance correlation coefficient to evaluate reproducibility, *Biometrics* 45 (1) (1989) 255–268, <https://doi.org/10.2307/2532051>.
- [35] F. Pedregosa, et al., Scikit-learn: machine learning in Python, *J. Mach. Learn. Res.* 12 (85) (2011) 2825–2830.
- [36] F. Chollet, Keras: the python deep learning library, *Astrophys. Source Code Lib.* (2018) ascl:1806.022Jun.
- [37] M. Teague, 'Image analysis via the general theory of moments', 1980, doi:10.1364/JOSA.70.000920.
- [38] J. Nunez-Iglesias, A.J. Blanch, O. Looker, M.W. Dixon, L. Tilley, A new Python library to analyse skeleton images confirms malaria parasite remodelling of the red blood cell membrane skeleton, *PeerJ* 6 (2018) e4312, <https://doi.org/10.7717/peerj.4312>. Feb.
- [39] K. Weiss, T.M. Khoshgoftaar, D. Wang, A survey of transfer learning, *J. Big Data* 3 (1) (2016) 9, <https://doi.org/10.1186/s40537-016-0043-6>. May.
- [40] J. Deng, W. Dong, R. Socher, L.-J. Li, K. Li, and L. Fei-Fei, 'ImageNet: a large-scale hierarchical image database', in *2009 IEEE Conference on Computer Vision and Pattern Recognition*, Jun. 2009, pp. 248–255. doi:10.1109/CVPR.2009.5206848.
- [41] A. Krizhevsky, 'Learning multiple layers of features from tiny images', p. 60, 2009.
- [42] K. He, X. Zhang, S. Ren, and J. Sun, 'Identity mappings in deep residual networks'. arXiv, Jul. 25, 2016. doi:10.48550/arXiv.1603.05027.
- [43] M. Tan and Q.V. Le, 'EfficientNet: rethinking model scaling for convolutional neural networks'. arXiv, Sep. 11, 2020. doi:10.48550/arXiv.1905.11946.
- [44] X. Glorot and Y. Bengio, 'Understanding the difficulty of training deep feedforward neural networks', in *Proceedings of the Thirteenth International Conference on Artificial Intelligence and Statistics*, JMLR Workshop and Conference Proceedings, Mar. 2010, pp. 249–256. Accessed: Nov. 09, 2023. [Online]. Available: <https://proceedings.mlr.press/v9/glorot10a.html>.
- [45] K. Team, 'Keras documentation: keras Applications'. Accessed: Jul. 26, 2022. [Online]. Available: <https://keras.io/api/applications/>.
- [46] S. Sawatzki, T.G. Woodcock, K. Güth, K.-H. Müller, O. Gutfleisch, Calculation of remanence and degree of texture from EBSD orientation histograms and XRD rocking curves in Nd-Fe-B sintered magnets, *J. Magn. Magn. Mater.* 382 (2015) 219–224, <https://doi.org/10.1016/j.jmmm.2015.01.046>. May.
- [47] S.I. Wright, M.M. Nowell, S.P. Lindeman, P.P. Camus, M. De Graef, M.A. Jackson, Introduction and comparison of new EBSD post-processing methodologies, *Ultramicroscopy* 159 (2015) 81–94, <https://doi.org/10.1016/j.ultramic.2015.08.001>. Dec.
- [48] R. Shwartz-Ziv, A. Armon, Tabular data: deep learning is not all you need, *Inf. Fusion* 81 (2022) 84–90, <https://doi.org/10.1016/j.inffus.2021.11.011>. May.
- [49] 'ImageNet: a large-scale hierarchical image database | IEEE Conference Publication | IEEE Xplore'. Accessed: Aug. 23, 2022. [Online]. Available: <https://ieeexplore.ieee.org/document/5206848>.
- [50] R. Löffler, D. Goll, G. Guth, T. Bernthaler, V. Pusch, G. Schneider, Lichtmikroskopische Analyse der intrinsischen Eigenschaften hart- magnetischer Phasen aus der Domänenstruktur, *Carl Zeiss Microsc. GmbH* (2013). White paperApr.
- [51] S.S. van Nielen, T.J. Verhagen, and R. Kleijn, 'Towards neodymium recycling: analysis of the availability and recyclability of European waste flows – supplementary information', *J. Clean. Prod.*, vol. 394, doi:https://doi.org/10.1016/j.jclepro.2023.136252.